ORIGINAL ARTICLE

Architectured van der Waals epitaxy of ZnO nanostructures on hexagonal BN

Hongseok Oh[1,5], Young Joon Hong[2,5], Kun-Su Kim[3], Sangmoon Yoon[3], Hyeonjun Baek[1], Seoung-Hun Kang[4], Young-Kyun Kwon[4], Miyoung Kim[3] and Gyu-Chul Yi[1]

Heteroepitaxy of semiconductors on two-dimensional (2-d) atomic layered materials enables the use of flexible and transferable inorganic electronic and optoelectronic devices in various applications. Herein, we report the shape- and morphology-controlled van der Waals (vdW) epitaxy of ZnO nanostructures on hexagonal boron nitride (hBN) insulating layers for an architectured semiconductor integration on the 2-d layered materials. The vdW surface feature of the 2-d nanomaterials, because of the surface free of dangling bonds, typically results in low-density random nucleation–growth in the vdW epitaxy. The difficulty in controlling the nucleation sites was resolved by artificially formed atomic ledges prepared on hBN substrates, which promoted the preferential vdW nucleation–growth of ZnO specifically along the designed ledges. Electron microscopy revealed crystallographically domain-aligned incommensurate vdW heteroepitaxial relationships, even though ZnO/hBN is highly lattice-mismatched. First-principles theoretical calculations confirmed the weakly bound, noncovalent binding feature of the ZnO/hBN heterostructure. Electrical characterizations of the ZnO nanowall networks grown on hBN revealed the excellent electrical insulation properties of hBN substrates. An ultraviolet photoconductor device using the vdW epitaxial ZnO nanowall networks/ hBN heterostructure was further demonstrated as an example of hBN substrate-based device applications. The architectured heteroepitaxy of semiconductors on hBN is thus expected to create many other device arrays that can be integrated on a piece of substrate with good electrical insulation for use in individual device operation.

INTRODUCTION

Heteroepitaxy of semiconductors on two-dimensional (2-d) layered nanomaterials has become a new integration method for fabricating transferable[1,2] and flexible[3–5] electronic and optoelectronic devices. Among various 2-d layered nanomaterials,[6,7] hexagonal boron nitride (hBN), a dielectric insulator with a wide direct bandgap of 5.2–5.9 eV, possesses great advantages as a substrate for many advanced electronics and optoelectronics[8,9] owing to its excellent thermal conductivity, optical properties,[10] chemical/mechanical stability[11] and low dielectric constant.[12] Because of the diatomic honeycomb crystal lattices of 2-d layered hBN sheets, the hBN can be structurally compatible with many semiconductors having wurtzite, zinc blende and diamond structures.[2] The atomic layered structure of hBN is also well suited as a substrate for transferable[2] and flexible device applications. Moreover, the ability of hBN to form alloy[13] or lateral heterostructures[14] with graphene is noteworthy for fabricating sophisticated on-demand devices. The recent progress of large-scale hBN synthesis with precisely controlled thickness *via* chemical vapor deposition techniques[11] may allow the integration of semiconductors with wafers based on conventional microfabrication processes. Accordingly, the heteroepitaxial integration of semiconductors on hBN is expected to generate significant advances in design, fabrication and performance for diverse semiconductor optoelectronic and electronic circuitry.

Noncovalent epitaxy, the so-called van der Waals (vdW) epitaxy,[15–18] has the ability to produce single-crystalline semiconductor nanostructures with an abrupt clean heterointerface and suppressed threading dislocation density, even for highly lattice-mismatched heteroepitaxial systems.[19] Accordingly, it is well suited for fabricating high-quality epitaxial semiconductor/hBN heterostructures for diverse device applications. Nevertheless, the weak attraction due to the chemically inert vdW surfaces makes it difficult to control the heterogeneous nucleation at specific sites; thus, amorphous open-patterned mask layers were used to direct the semiconductor nucleation on the vdW surfaces.[20,21] In addition, a major challenge remains in the vdW epitaxy of semiconductors on hBN: precise control of the position, size and shape of the semiconductor nanostructures, all of which are critical for monolithic microelectronic processing.[22–26] In this article, we report on the maskless shape-controlled vdW

[1]Department of Physics and Astronomy, Institute of Applied Physics, Seoul National University, Seoul, Korea; [2]Department of Nanotechnology and Advanced Materials Engineering, Graphene Research Institute, and Hybrid Materials Research Center, Sejong University, Seoul, Korea; [3]Department of Materials Science and Engineering, Seoul National University, Seoul, Korea and [4]Department of Physics, Research Institute of Basic Science, Kyung Hee University, Seoul, Korea
[5]These authors contributed equally to this work.
Correspondence: Professor G-C Yi, Department of Physics and Astronomy, Institute of Applied Physics, Seoul National University, 1 Gwanak-ro, Gwanak-gu, Seoul 151-747, Korea.
E-mail: gcyi@snu.ac.kr
Received 12 August 2014; revised 24 September 2014; accepted 29 September 2014

heteroepitaxy of ZnO nanostructures on hBN substrates in a designed manner using the artificially formed atomic ledges on hBN. Electron microscopic analyses and first-principles theoretical calculations exhibit how the highly lattice-mismatched ZnO/hBN heterojunction is fabricated to be of high quality using vdW epitaxy. The role of the atomic ledges of hBN in controlling the morphology and shape of the semiconductor overlayer is discussed. The ultraviolet (UV) photosensor device using the vdW epitaxial ZnO nanowall networks/hBN heterostructure is further demonstrated as an example of hBN substrate-based device applications.

MATERIALS AND METHODS
vdW heteroepitaxy of ZnO nanostructures on hBN
ZnO nanostructures were grown on hBN films by vdW epitaxy using metal–organic vapor-phase epitaxy (MOVPE). For substrate preparation, hBN layers were transferred onto SiO_2/Si substrates by the mechanical exfoliation method. To obtain shape-controlled ZnO nanowalls, the hBN layers were treated by O_2 (or Ar) plasma with an RF power of 50 W and an O_2 (or Ar) partial pressure of 100 mTorr. Prior to ZnO growth, thermal hydrogenation of the hBN layers was conducted at 500–700 °C for 30 min in an ambient H_2/Ar gas mixture to prevent oxidation of the ledges and to passivate the dangling bonds of ledges with ' – H'. The stability of the hydrogenated hBN ledge is the key to the vdW epitaxy. According to theoretical computations, the binding energy of hydrogenated hBN was determined to be − 1.04 eV per atom,[27] suggesting that the hydrogenation is stable and can be readily formed by the reaction with hydrogen at high temperatures. Immediately after the hydrogenation process, the vdW–MOVPE of the ZnO nanostructures was performed. High-purity diethylzinc and oxygen were used as the reactants for Zn and O, respectively, and high-purity argon was used as a carrier gas. The flow rates of diethylzinc and oxygen were 20 and 100 sccm, respectively. To prevent oxidation of the hBN layers, diethylzinc was allowed to flow into the reactor before the injection of O_2. The vdW growth of the ZnO nanostructures was typically performed at a growth temperature of 500–700 °C and a reactor pressure of ~ 3.0 Torr for 60 min.

Substrate preparation for selective growth of ZnO nanowalls on hBN
Selective-area oxygen plasma treatment was performed using a patterned poly-methyl methacrylate mask. The patterned poly-methyl methacrylate layer was spin-coated onto the hBN, and the hole patterns were formed by electron-beam lithography, which was followed by an oxygen plasma treatment to define the selectively treated areas. After plasma treatment, the patterned poly-methyl methacrylate layer was removed by acetone in a bath for over 12 h.

Device fabrications and measurements
To fabricate devices for electrical characterizations, ZnO nanowall networks grown on hBN substrates were used. The electrodes were defined by electron-beam lithography, and Ti/Au (100/150 nm) contact layers were deposited using electron-beam evaporation. The UV photosensor device of the ZnO nanowall/hBN was fabricated by making two Ohmic contacts of Ti/Au pads on the ZnO nanowalls. The electrical properties of the ZnO nanowalls/hBN were characterized by measuring currents and voltages and creating current–voltage (I–V) characteristic curves. In the photodetection experiments, the photocurrent was measured through monitoring the change of current in response to irradiation of the UV lights with a fixed bias of 1.0 V. The mercury/argon lamp (< 5 W, Hg(Ar) lamp, Model 6035, Newport Corporation, Irvine, CA, USA) was used as a UV photogeneration source.

Characterizations
The morphological and microstructural characteristics of the ZnO nanostructures on hBN were investigated using field-emission scanning electron microscopy and high-resolution transmission electron microscopy, respectively. For cross-sectional transmission electron microscopy (TEM) imaging and electron diffraction analyses, samples were milled using a focused ion beam

machine. The acceleration voltage of the TEM (FEI Tecnai G^2 F20, FEI company, Hillsboro, OR, USA) observation was 200 keV. The incidence electron beam was directed along the ZnO [11$\bar{2}$0] orientation to define the crystal structure of the ZnO nanostructures. The polarity of the ZnO nanostructures was determined using a convergence beam electron diffraction technique and confirmed by the JEMS simulation package (JCPDS 36–1451). For plan-view TEM observations, the hBN-transferred holey carbon TEM grid was employed as a substrate.[28] The optical properties of the ZnO nanostructures were characterized by both cathodoluminescence (CL, Gatan MonoCL3+, Gatan Inc., Pleasanton, CA, USA) and photoluminescence spectroscopy. The CL images and spectra were recorded at room temperature using a 10-kV electron beam.

Theoretical calculations
A first-principles calculation based on density-functional theory (DFT) was performed using the Vienna *ab initio* simulation package[29] to study the electronic structures of the ZnO/BN heterostructure. We used the Perdew–Burke–Ernzerhof[30] functional based on a generalized gradient approximation for the exchange correlations and the projector-augmented wave method for the descriptions of core electrons. The DFT-D2 method of Grimme[31] was also used to consider the London dispersion interactions between the ZnO and BN sheet. Plain-wave basis sets were used with a plain-wave cutoff of 500 eV. Brillouin-zone integrations were performed on a grid of $2 \times 2 \times 1$ Monkhorst-Pack special points. To model the ZnO/BN heterointerface, we used the $3 \times 3 \times 2$ ZnO on the 4×4 BN sheet with a vacuum region larger than 15 Å. The topmost O layer was passivated with hydrogen atoms. Because the slab system was asymmetric along the z direction, a dipole correction was considered. All atoms were relaxed by the conjugate gradient method until none of the remaining Hellmann-Feynman forces acting on any atoms exceeded 0.03 eV Å^{-1}.

RESULTS AND DISCUSSION
Morphology of ZnO grown on hBN
The vdW heteroepitaxy of ZnO using MOVPE yielded two distinct nanostructure morphologies on hBN. The schematics in Figure 1 represent the experimental procedures for obtaining either ZnO nanoneedles or nanowalls depending upon the surface treatment of hBN. Under the same vdW–MOVPE growth conditions, the pristine hBN surface resulted in vertical ZnO nanoneedle arrays (Figures 1a and b), while O_2 or Ar plasma-treated hBN substrates yielded high-density vertical nanowall networks (Figures 1c and d). The number density of nanoneedles was measured to be $(6.2 \pm 2.8) \times 10^8$ cm^{-2}; the line density of nanowall networks was $(1.5 \pm 0.2) \times 10^5$ cm^{-1} (corresponding to $\approx 2.3 \times 10^{10}$ cm^{-2} in areal density). This outcome suggests that the plasma-treated hBN surface promotes high-density heterogeneous vdW nucleation leading to the formation of interconnected nanowalls, presumably resulting in a random network morphology. Because both Ar and O_2 plasma treatments damage and etch the hBN surfaces (Supplementary Figure S1), the roughness, including the atomic steps and kinks, formed by plasma is thought to play a critical role in the control of nanostructure density and morphology (Supplementary Figure S2). This phenomenon implies that artificially controlled atomic steps or kinks of hBN enable the growth of nanostructures with designed shapes, which will be demonstrated later.

We envision that ZnO nanoneedles are grown on quite tiny atomic edges (or vacancies) of hBN whereas the nanowalls are grown along the long ledges that are the contoured continuum of the atomic step-edges. On the mechanically exfoliated pristine hBN substrates, three different morphologies of ZnO nanostructures were obtained by the vdW epitaxy: (i) isolately grown nanoneedles, (ii) high-density nanoneedles and (iii) nanowalls with high-density nanoneedles formed in an alignment (Supplementary Figure S3). As there are many long

step-edges on the exfoliated hBN layers, it is surmised that the isolated nanoneedles were formed on the flat hBN terrace region, whereas the high-density formation of nanoneedles along the ledges became interconnected to form the nanowalls.

Microstructure of vdW heteroepitaxial ZnO/hBN

The vdW heterointerface and crystallographic growth direction of the ZnO nanostructures were examined by cross-sectional high-resolution TEM. The TEM images of Figures 2a and b show that a ZnO nanoneedle grew vertically on hBN layers with an atomically abrupt heterointerface. From the high-resolution TEM image, the lattice spacings between the adjacent planes were measured to be 0.26 and 0.34 nm in the ZnO nanoneedle and hBN layer, corresponding with the *d*-spacings of ZnO(0002) and hBN(0002), respectively. Fast

Fourier-transformed micrographs in the insets of Figure 2b show that the ZnO nanoneedle grew along the *c* axis of the wurtzite perpendicular to the hBN surface. Importantly, no extended crystal defects, such as threading dislocations and stacking faults, were observed at the heterointerface through high-resolution and two-beam microscopic analyses; this is presumably due to stress relaxation through the noncovalent vdW heterointerface. The previous works by Utama *et al.*[19] clarified that no misfit threading dislocations are generated from the highly incommensurate vdW heteroepitaxial system. Hence, all the microstructural features showed that the high-quality heterointerfaces of the single-crystalline ZnO nanostructure/hBN are presumably attributed to the weakly bound vdW heterojunction.

The convergence beam electron diffraction analyses revealed notable microstructural characteristics of vdW epitaxial ZnO/hBN. Figure 2c
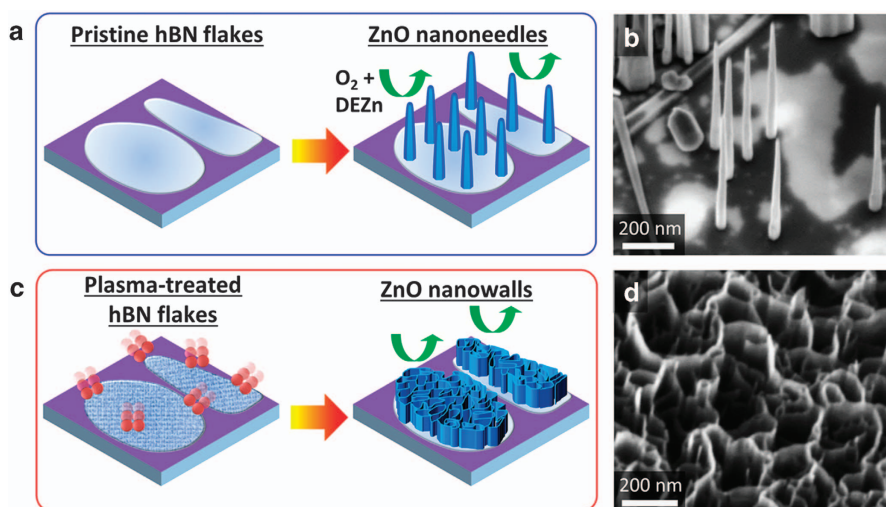

Figure 1 Morphology-controlled vdW heteroepitaxy of ZnO nanostructures on hBN substrates. Schematic of the fabrication process and tilt-view field-emission scanning electron microscopy images of (**a** and **b**) ZnO vertical nanoneedle arrays and (**c** and **d**) nanowall networks. ZnO nanoneedles and nanowall networks were obtained using pristine hBN and plasma-treated hBN substrates, respectively.
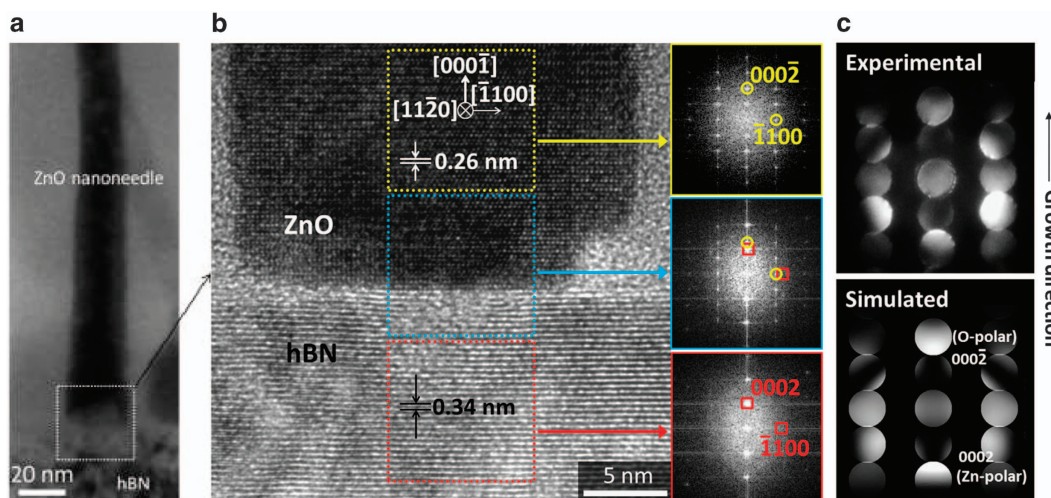

Figure 2 Heterointerface of vdW epitaxial ZnO/hBN observed by cross-sectional TEM. (**a**) Low-magnification cross-sectional TEM image of vertical ZnO nanoneedles grown on hBN. (**b**) high-resolution transmission electron microscopy lattice images of the ZnO nanoneedle/hBN heterointerface. The right insets are selected-area diffraction patterns obtained through Fast Fourier-transformed processing of the high-resolution transmission electron microscopy images marked with the enclosed areas. (**c**) Experimental and simulated convergence beam electron diffraction patterns of the ZnO nanoneedles preferentially grown along the O-polar (000$\bar{1}$) direction.

shows that the convergence beam electron diffraction disk patterns obtained from the ZnO nanoneedle exhibit clear asymmetric stripy contrasts: the ZnO nanoneedles were found to grow along the oxygen-terminated $[000\bar{1}]$ direction by vdW heteroepitaxy on hBN, which is in close accordance with those simulated at the same sample thickness (~25 nm). Noticeably, ZnO nanowalls on plasma-treated hBN also exhibited identical growth orientation (Supplementary Figure S6). These convergence beam electron diffraction analyses obtained from the nanoneedles and nanowalls grown on hBN indicate that ZnO nanostructures grow exclusively along the oxygen-polar c axis direction through vdW heteroepitaxy regardless of the surface treatment of hBN.

The vdW heteroepitaxial relationship of the ZnO nanostructures and hBN was further investigated by plan-view TEM observations. The low-magnification TEM image of ZnO nanoneedles grown on few-layer hBN films shows that the neighboring nanoneedles, all of which exhibit a hexagonal prismatic morphology with six wurtzite-$\{10\bar{1}0\}$ sidewall facets, have a fairly uniform sixfold rotational in-plane alignment (Figure 3a). The high-resolution TEM images in the insets of Figure 3b display the hexagonal lattices of ZnO and hBN with the same crystallographic alignments, although the lattice mismatch of ZnO/hBN is -30.0% for the heteroepitaxial relationship of $(000\bar{1})$ $[10\bar{1}0]_{ZnO} \| (0001)[10\bar{1}0]_{hBN}$. It is well known that such large lattice misfits in a hexagonal heteroepitaxial system, for example, ZnO/Al$_2$O$_3$, GaN (or AlN)/Al$_2$O$_3$, etc., typically yield the heterostructures of $(0001)[11\bar{2}0]_{overlayer} \| (0001)[10\bar{1}0]_{substrate}$, whose overlayer is

crystallographically rotated by 30° with respect to the substrate to minimize dangling bond density through covalent heteroepitaxy.[32–34] Recent works on epitaxy of III–V nanowires on graphene also discussed the possible rotated in-plane epitaxial relationships or different nanowire growth directions presumably caused by lattice mismatch when covalent epitaxial links exist at the heterointerface.[35,36] Hence, it is strongly suggested that the observed domain-aligned heteroepitaxial relationship of ZnO/hBN should result from weakly bound vdW heterointerfaces.

The plan-view TEM image in Figure 3b shows the presence of periodic triangular Moiré fringes in the ZnO/hBN with a periodicity of ~1.0 nm because of the large lattice misfits. The periodicity was three times as large as the lattice constant of ZnO (a ≈ 3.25 Å) and four times as large as the lattice constant of hBN (a ≈ 2.50 Å). These values for the Moiré periodicity, however, have a misfit of 2.5% so that the ZnO/hBN is classified as an incommensurate vdW epitaxial system.

The selected-area electron diffraction patterns in Figure 3c, obtained from a few dozen nanoneedles within a selected area with an aperture size of ~200 nm, shows the homogeneous heteroepitaxial relationship of ZnO/hBN. No multiple epitaxial relationships were observed in the plan-view TEM analysis, and the statistical distribution of the in-plane alignment of ZnO nanoneedles was estimated at a standard deviation width of ±4.5° in the selected-area electron diffraction intensity profile of ZnO $\{10\bar{1}0\}$ (Figure 3d). We believe that the slightly deviated epitaxial relationship is presumably caused by the weekly bound attraction of the vdW epitaxial ZnO/hBN heterointerface.
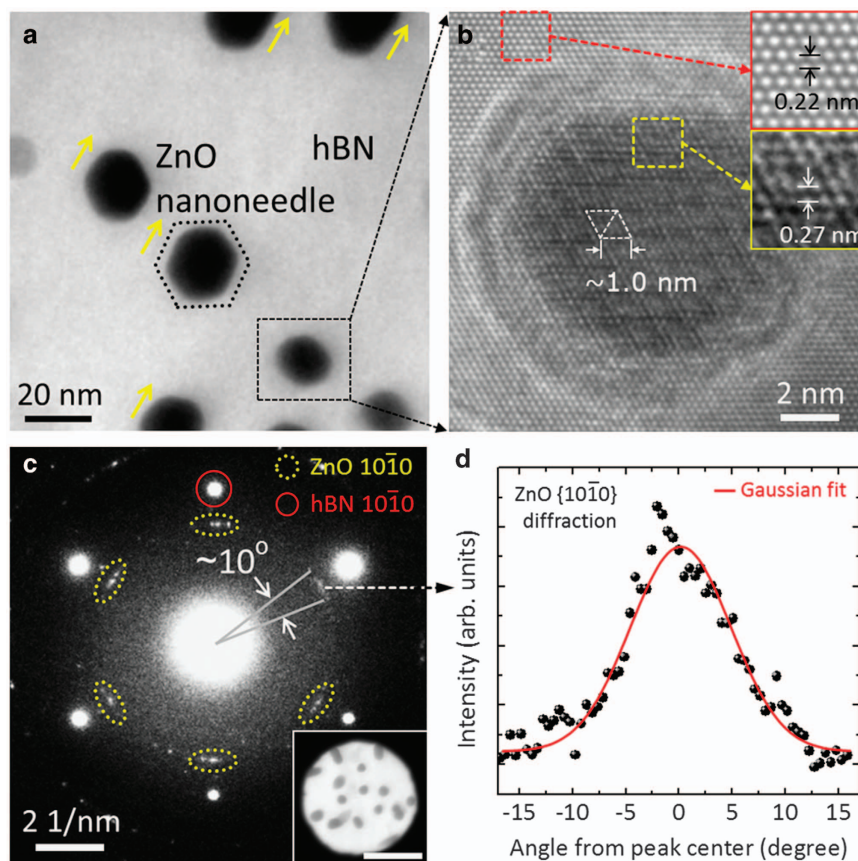

Figure 3 vdW heteroepitaxial relationship of ZnO/hBN investigated by plan-view TEM. (**a**) Plan-view low-magnification TEM image of ZnO nanoneedles grown on few-layer hBN. (**b**) Plan-view high-resolution transmission electron microscopy lattice image displaying in-plane epitaxial relationship of ZnO/hBN. Diamond-shape Moiré patterns are repeatedly observed every 1 nm. (**c**) Selected-area electron diffraction patterns obtained from the area shown in the inset (scale bar, 100 nm). (**d**) Intensity profile of the electron beam diffraction of ZnO $(10\bar{1}0)$ as a function of the central angle.

Atomic configuration at the vdW ZnO/hBN heterointerface

On the basis of the TEM observations, a ball-and-stick model was simulated with an assumption that the ZnO/hBN interfacial layers are fully relaxed, owing to weakly bound vdW heteroepitaxy. The low-magnification ball-and-stick image clearly displays regular triangular Moiré patterns with a periodicity of ~ 1.0 nm (Figures 4a and c). This result is in close agreement with the plan-view TEM observation shown in Figure 3b. The corresponding simulated diffraction patterns (Figure 4b), obtained through Fourier transforms from the ball-and-stick image of Figure 4a, are also in good agreement with the selected-area electron diffraction pattern shown in Figure 3c. Inside a unit Moiré pattern (marked with a triangle in Figure 4c), two distinct heteroepitaxial atomic configurations are shown: ball-to-ball and ball-to-hollow epitaxial atomic configurations (Figure 4d). According to the ball-and-stick model, there are at least a few plausible epitaxial arrangements because of the incommensurate epitaxial relationship, as displayed in Figure 4e.

vdW heterointerface of ZnO/hBN simulated by DFT

The vdW interfacial binding properties of the epitaxial ZnO/hBN heterostructures were explored by DFT total energy and electronic structure calculations. Two representative supercells are presented in Figures 5a and b: a ball-top-matching configured supercell in which two Zn atoms are on top of B and/or N atoms (type I, Figure 5a); and a hollow-matching supercell consisting of two hollows of ZnO hexagon lattices on top of B or N atoms (type II, Figure 5b) in a supercell of a ZnO slab (3×3) on a BN slab (4×4).

The DFT computations for these two supercells revealed a few important interfacial features. First, the interaction energy $(\Delta E = E_{total} - E^{ZnO} - E^{hBN})$ values of both type I and II supercells were calculated to be 2.170 and 2.165 eV nm^{-2}, respectively. These values are much smaller than those of typical covalent bindings by one or two orders of magnitude. Importantly, the differences in the interfacial interaction energies were quite small (5 meV nm^{-2}) between the type I and II supercells. Second, the equilibrium vdW spacing of ZnO–hBN was
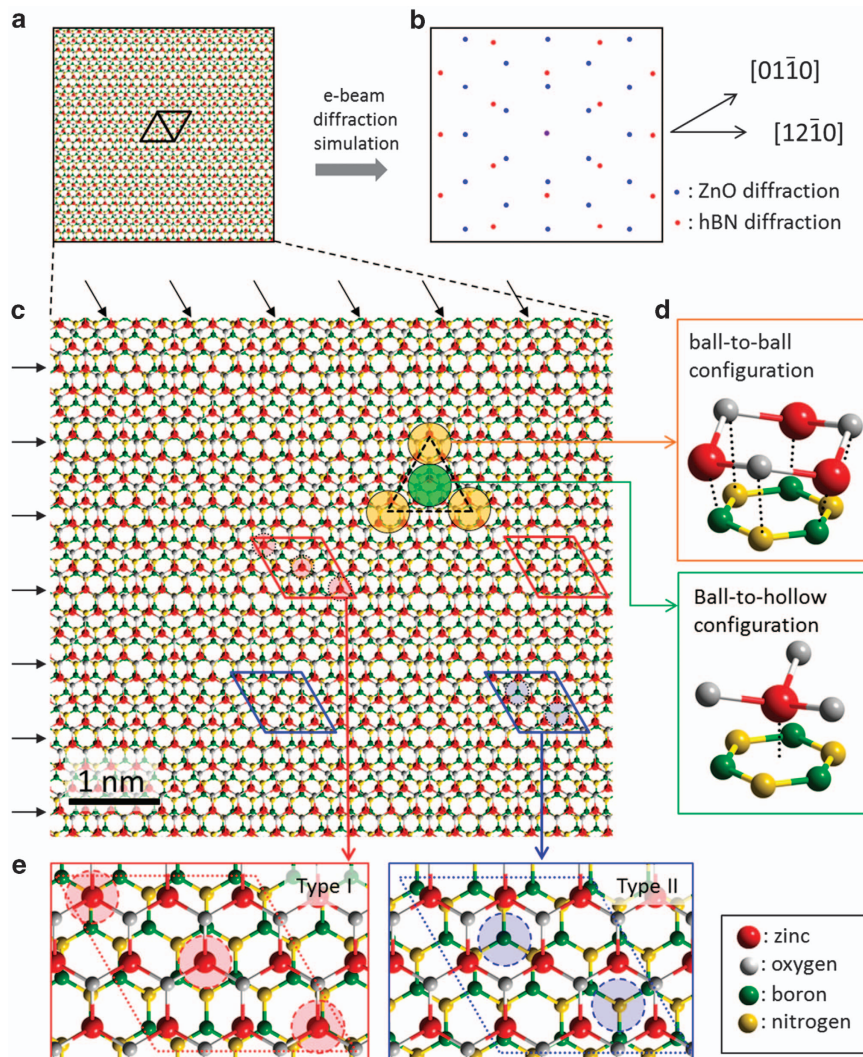

Figure 4 Ball-and-stick model for vdW epitaxial ZnO/hBN heterostructure. (**a**) Low-magnification model for $(000\bar{1})[10\bar{1}0]ZnO \parallel (0001)[10\bar{1}0]hBN$ heterostructure viewed along [0001]. The image clearly exhibits periodic triangular Moiré fringes with a periodicity of ~ 1.0 nm. (**b**) Diffraction patterns obtained through a Fourier-transform-based simulation. (**c**) High-magnification ball-and-stick model. (**d**) Two heterointerfacial atomic epitaxial relationships for the ball-to-ball (upper panel) and ball-to-hollow (bottom panel) configurations appearing in the Moiré pattern. (**e**) Two supercell structures of ball-top-matching (type I) and hollow-matching (type II) (3×3)–ZnO/(4×4)-BN heterojunctions for the incommensurate vdW ZnO/hBN heterostructure.
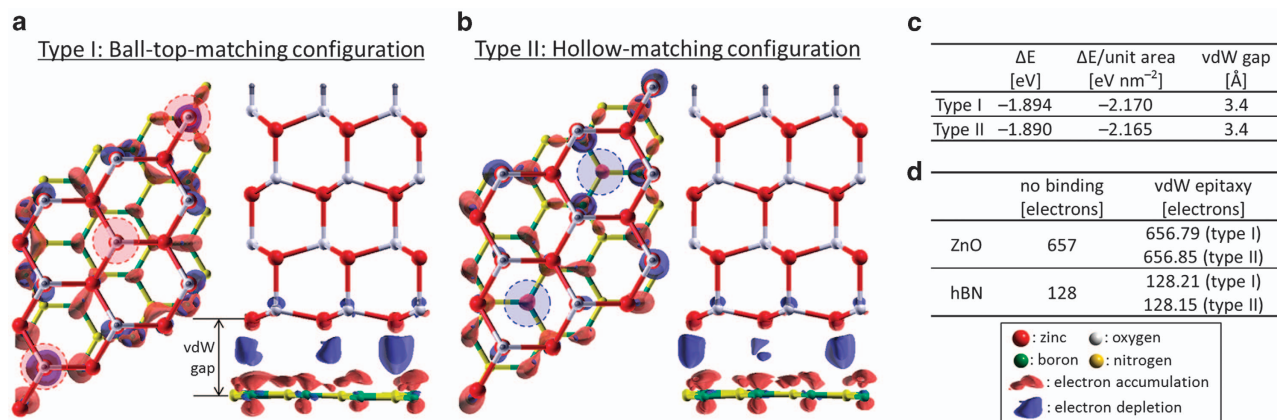
Figure 5 Electronic structure and adhesion energy of the vdW epitaxial ZnO/hBN heterointerface computed by the DFT method. Atomic model structures and electron density difference isosurfaces at the periphery of the heterointerfaces with (**a**) ball-top-matching and (**b**) hollow-matching configurations of ZnO/hBN. The electron density was contoured with an isovalue of $\pm 0.0002 \, e\,\text{Å}^{-3}$. (**c**) vdW heterointerfacial adhesion energy and equilibrium vdW distance values for type I and II supercells. (**d**) The electron populations in the ZnO and hBN parts of the supercells before and after vdW epitaxy, calculated by Bader analysis. The electronic structure mapped at the ZnO/hBN heterointerface implies a vdW binding feature with less electron orbital hybridization.

3.4 Å (Figure 5c), which is greater than the typical distances of chemical primary bonds, such as covalent or ionic bonds. Third, the heterointerface for both type I and II supercells exhibited no bonds with valence electrons being shared or donated (Figure 5d). The electron density difference contoured at $\pm 0.0002 \, e\,\text{Å}^{-3}$ (Figures 5a and b) and Bader analysis (Figure 5d) showed little electron orbital hybridization (charge transfer) through the vdW heterointerface. At equilibrium, little buckling (or distortion) was observed at the heterointerfaces. Notably, the calculated values for type I and II supercell heterointerfaces showed negligible disparities in terms of binding energy, equilibrium vdW distance and electronic structure. This outcome implies that there is no primary epitaxial relationship among type I and II supercell heterointerfaces. Therefore, all of the calculated heterointerfacial results show that the binding interactions are almost homogeneous over the entire ZnO/hBN heterointerface.

Nanoarchitectural vdW heteroepitaxy of ZnO on hBN
The preferential formation of high-density nanowalls on the rough hBN surface could be exploited for creating shape- and position-controlled ZnO nanostructures. Figure 6a shows schematics of the process for selective-area vdW–MOVPE of ZnO nanowalls. To control both the shape and position of the ZnO nanowalls, the predetermined area of hBN was treated by O_2 (or Ar) plasma through the opening of a resist layer patterned by conventional lithography and followed by the wet removal of the polymer resist for high-temperature growth.

The scanning electron microscopy images of Figures 6b and c shows the shape- and position-controlled ZnO nanostructures composed of vertical nanowall networks. The shapes of the outer nanowalls were determined by the plasma-treated area of hBN. Specifically, the outer nanowalls are continuously interconnected with uniform heights even in complicated shapes because of the enhanced growth of ZnO nanowalls along the ledges of the plasma-treated hBN area. Shape-controlled ZnO nanowall architectures grown on hBN exhibited the same epitaxial relationship of $(000\bar{1})[10\bar{1}0]_{ZnO} \parallel (0001)[10\bar{1}0]_{hBN}$ and exclusive growth orientation along the oxygen-terminated $[000\bar{1}]$ direction as individual ZnO nanoneedles grown on pristine hBN layers (Supplementary Figure S6).

The optical properties of the ZnO nanoarchitectures were investigated using CL spectroscopy. The room-temperature CL spectrum of the ZnO nanostructure arrays shows a dominant near-band-edge emission peak at 3.25 eV, attributable to a free exciton emission (Figure 6e).[37] No deep-level emission, typically observed from bulk ZnO materials, was observed. The full width at half maximum of the near-band-edge was as narrow as ~ 100 meV, which is comparable with a previous report,[38] indicating the high quality and purity of the ZnO nanostructures grown on hBN by vdW epitaxy. The insets of Figure 6e show the scanning electron microscopy and corresponding CL monochromatic images of the ZnO nanostructure array. The latter was measured at the photon energy of 3.25 ± 0.01 eV using a monochromator. The monochromatic CL image shows homogeneous and strong CL emission of the ZnO nanostructure arrays. The scanning electron microscopy and CL images look almost the same, suggesting that nonradiative or other radiative transitions caused from defects or impurities were not observed. The near-band-edge emissions of the nanostructure arrays were homogeneous in intensity. Additionally, nitrogen- or boron-associated ZnO luminescence was not observed from the high-resolution photoluminescence spectroscopic analyses (Supplementary Figure S5).[39,40] This suggested that the atoms in hBN were not incorporated into the ZnO nanostructures during the vdW–MOVPE process.

The vdW–MOVPE growth mode of ZnO was altered from 1-d nanoneedle formation to vertical 2-d nanowall growth as the surface of the hBN was roughened by the plasma treatment. This vdW growth mode transition is strongly related to the atomic ledges formed on the hBN surface by the plasma. According to our investigations (Supplementary Figures S1 and S2), it is envisioned that the hBN ledges formed by plasma treatment promote the formation of high-density ZnO nuclei along the ledges, resulting in continuously interconnected ZnO nanowalls. This plausible scenario could be applied to the architectural vdW epitaxy of ZnO nanostructures. Because of the slow plasma etching rate of hBN (~0.5–0.8 Å s^{-1}), shape-controlled atomic ledges could be formed with a precisely controlled etching depth at the few-atomic-layer level (Figure 6d and Supplementary Figure S4). During the vdW–MOVPE process, multiple ZnO nuclei that preferentially dwell along the vdW ledges (the edge of the plasma-treated area) are then connected at their base to form outer nanowalls.

The enhanced nucleation of ZnO along the ledges points to the existence of a reduced Ehrlich–Schwoebel energy barrier encountered by the adatoms that diffuse downward[41,42] from the non-treated
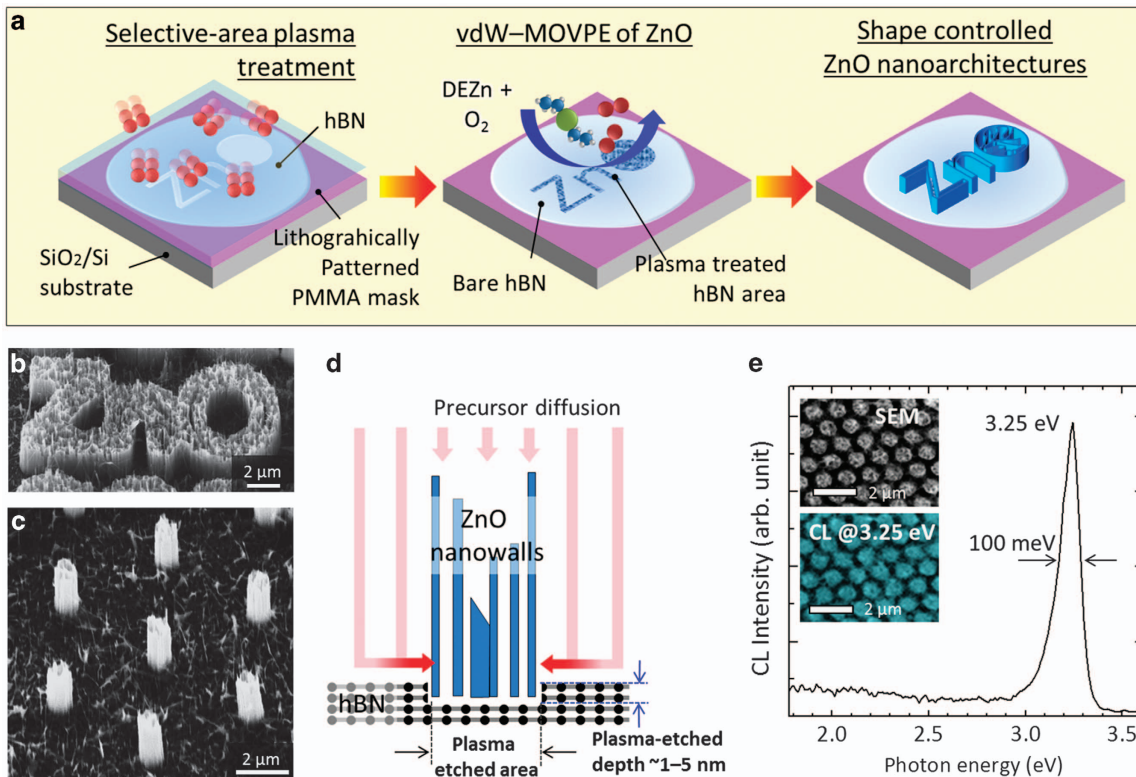
Figure 6 Shape-controlled vdW heteroepitaxy of ZnO nanoarchitectures on hBN layers. (a) Schematic of selective growth of ZnO nanowalls on hBN films for shaping the outer nanowalls. (b and c) Tilt-view scanning electron microscopy image of ZnO nanoarchitectures on hBN films with designed shape and spatial arrangements. (d) Cross-sectional schematic showing how ZnO nanoarchitectures are formed on a plasma-treated hBN area *via* vdW–MOVPE. (e) Room-temperature CL spectra of ZnO nanostructures. The insets are top-view scanning electron microscopy images (upper) and the corresponding monochromatic CL image obtained at a photon energy of 3.25 eV (bottom).

ultraflat hBN area into the plasma-etched rough hBN in the initial vdW growth stage. The reduced barrier presumably played a critical role in overcoming the difficulties of heterogeneous nucleation at specific sites caused by the weak attraction of the chemically inert vdW surface. Consequently, the shape-controlled semiconductors could be created by maskless vdW heteroepitaxy along the artificially formed ledges, which is distinguishable from the conventional selective-area growth that necessarily uses amorphous growth mask layers.[43] The high-density formation of nanowalls on the hBN flake entirely etched by plasma also supports our argument on the reduced energy barrier for the enhanced nucleation of ZnO along the ledges because longer plasma exposure causes formation of more ledges on the hBN flake (Supplementary Figures S1 and S2). Importantly, the ZnO nanowalls grown by the architectured vdW heteroepitaxy were single crystalline, as confirmed by TEM analysis (Supplementary Figure S6b), indicating that no other directional growth occurred from the ledges. This finding implies that the maskless vdW selected-area heteroepitaxy of shape-controlled ZnO nanostructures is a suitable integration method for use in electronic and optoelectronic device applications. It is also expected that the selective vdW epitaxy can be exploited for fabricating smooth ZnO thin film structures by combining two processes required to grow the film structures: (i) formation of high-density regular arrays of nuclei (or nanostructures) that are sufficiently close to coalesce to form films, and (ii) epitaxial lateral overgrowth on the site-selectively formed nanostructures. Notably, Liu and co-workers[44] reported that selected-area chemical surface modification inhibited growth, but only the intact substrate area contributed to the maskless

site-selective vdW epitaxy of Bi_2Se_3, Bi_2Te_3 and In_2Se_3[45] nanoplates with the desired spatial arrangements.

Electrical properties of ZnO nanowalls/hBN and UV photosensor devices

The electrical properties of the ZnO nanowall networks/hBN heterostructure were investigated by measuring *I–V* characteristic curves of the ZnO nanowall networks, the ZnO–hBN heterojunction and the bare hBN layer. For the measurements, four Ti/Au bilayer electrodes were prepared to comprise three different device configurations, as depicted in Figure 7a. The *I–V* curves of Figure 7b show that the ZnO nanowall networks with Ohmic Ti/Au electrodes exhibited a linear *I–V* relationship, suggesting a high degree of conductivity of the ZnO nanowall networks and good Ohmic contacts with the Ti/Au electrodes. According to our previous work on the thermoelectric power analyses, the carrier concentration of the undoped ZnO nanostructures grown under the same MOVPE conditions was measured to be $\sim 10^{18}\,cm^{-3}$.[46] Thus, the ZnO nanostructures grown on hBN are also expected to exhibit the same background carrier concentration. The bare hBN layer and ZnO nanowall–hBN heterostructure presented excellent insulating characteristics with a typical electrical leakage of $\sim 10^{-12}\,A$ under an applied bias voltage range of -5 to $5\,V$ (Figure 7b). The leakage current of the hBN layer and the ZnO/hBN heterojunction was lower (6 or 7 orders of magnitude) than the typical current measured from the ZnO nanowall networks with the same device dimension. This outcome strongly implies that the use of hBN substrates can be applied to individually operate the nanodevice
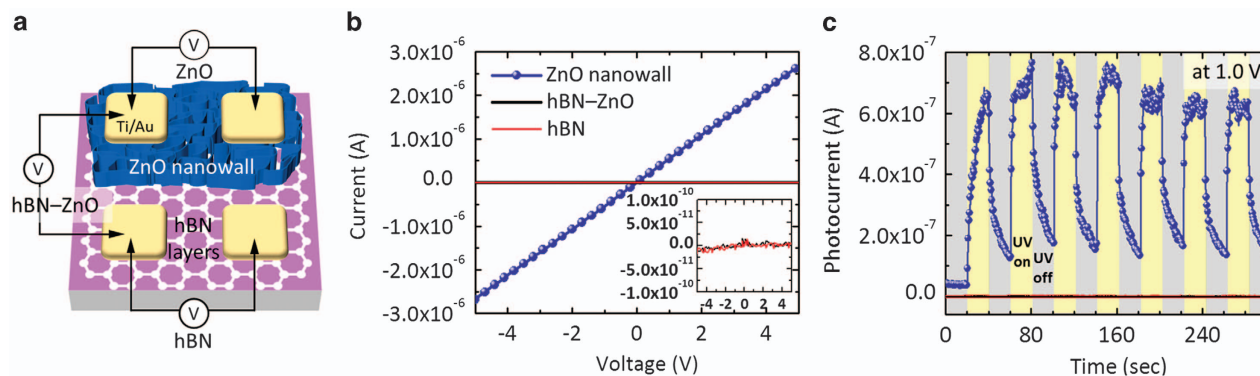
8

Figure 7 UV photosensor of a ZnO nanowall/hBN. (**a**) Schematics of the ZnO nanowall network/hBN photoconductor device with three different electrode configurations. (**b**) I–V characteristic curves for three different device configurations of the ZnO nanowall networks, the ZnO nanowall–hBN heterojunction, and the bare hBN layer measured in dark room conditions. Inset shows the I–V curves of the ZnO nanowall–hBN heterojunction (black solid line) and the bare hBN layer (red solid line). (**c**) Photoresponse characteristics measured at bias voltage of 1.0 V under alternate on/off cycles. Black and red solid lines are the photoresponse characteristics of ZnO nanowall–hBN heterojunction and the bare hBN layer, respectively.

arrays that are integrated on a piece of substrate for good electrical insulation from neighbor devices.

The UV photosensor devices were fabricated with three different electrode configurations. The dark and photoexcited currents were measured at various applied bias voltages of − 5.0 to 5.0 V (Supplementary Figure S7). The time-dependent photoresponses of the ZnO nanowall/hBN heterostructure devices were obtained at a bias of 1.0 V under duty-cycled on/off (20/20 s) UV irradiation. The UV irradiation from a mercury lamp drastically increased the electrical current of the ZnO nanowall photosensor (blue solid circles in Figure 7c). The mean on/off ratio of the photocurrent-to-dark current of the ZnO nanowall photodetector was measured to be ~ 4–5, indicating sensitive UV detection of the ZnO nanowall networks. In contrast, the other device configurations of the ZnO–hBN heterojunction and bare hBN layer exhibited no clear photoresponses (red and black lines in Figure 7c; Supplementary Figure S7), suggesting that the hBN is a good wide bandgap insulator sufficiently insensitive to the UV irradiation. Accordingly, the photogeneration occurred in the ZnO nanowalls and conduction through the nanowall networks significantly contributed to the photocurrent in the UV photosensor of the ZnO nanowall/hBN heterostructure. Notably, no obvious photoresponses were observed by indoor light illumination or white radiation from a halogen lamp, indicating that the UV photoconductor device of the ZnO nanowall networks/hBN is selectively sensitive only to UV light with a photon energy higher than the bandgap energy of ZnO.

CONCLUSION

A new approach for fabricating nanoarchitectured semiconductors on dielectric hBN layers was demonstrated using the vdW epitaxy of ZnO nanostructures and selective-area plasma etching of hBN. The electron microscopic observations exhibited homogeneous epitaxial formation of vertical, single-crystalline ZnO nanostructures on hBN with abrupt and clean heterointerfaces. The theoretical investigations showed no primary chemical binding features of epitaxial ZnO/hBN heterostructures with large interfacial spacing and small binding energy. Importantly, artificial atomic ledges of hBN, formed simply by selective plasma treatment, enabled the formation of ZnO nanostructures with designed shapes and spatial arrangements. The electrical characterizations revealed excellent electrical insulation properties of hBN substrates. An UV photosensor device of the ZnO nanowall networks/hBN demonstrated the feasibility of hBN substrate-based

device applications. The ability of the vdW heteroepitaxy to allow for shape-controlled vertical semiconductor nanostructures on insulating hBN represents a significant advance in the integration of semiconductors on 2-d nanomaterials. Generally, we believe that our route to integrating the semiconductor nanostructures epitaxially on hBN might be readily expanded to create many other semiconductors/layered insulating (or dielectric) nanomaterials for diverse electronic and optoelectronic device applications.

CONFLICT OF INTEREST
The authors declare no conflict of interest.

1 Chung, K., Lee, C.-H. & Yi, G.-C. Transferable GaN layers grown on ZnO-coated graphene layers for optoelectronic devices. Science **330**, 655–657 (2010).
2 Kobayashi, Y., Kumakura, K., Akasaka, T. & Makimoto, T. Layered boron nitride as a release layer for mechanical transfer of GaN-based devices. Nature **484**, 223–227 (2012).
3 Peng, H., Dang, W., Cao, J., Chen, Y., Wu, D., Zheng, W., Li, H., Shen, Z.-X. & Liu, Z. Topological insulator nanostructures for near-infrared transparent flexible electrodes. Nat. Chem. **4**, 281–286 (2012).
4 Lee, C.-H., Kim, Y.-J., Hong, Y. J., Jeon, S.-R., Bae, S., Hong, B. H. & Yi, G.-C. Flexible inorganic nanostructure light-emitting diodes fabricated on graphene films. Adv. Mater. **23**, 4614–4619 (2011).
5 Choi, D., Choi, M.-Y., Choi, W. M., Shin, H.-J., Park, H.-K., Seo, J.-S., Park, J., Yoon, S.-M., Chae, S. J., Lee, Y. H., Kim, S.-W., Choi, J.-Y., Lee, S. Y. & Kim, J. M. Fully

rollable transparent nanogenerators based on graphene electrodes. *Adv. Mater.* **22**, 2187–2192 (2010).

6 Osada, M. & Sasaki, T. Two-dimensional dielectric nanosheets: Novel nanoelectronics from nanocrystal building blocks. *Adv. Mater.* **24**, 210–228 (2012).

7 Butler, S. Z., Hollen, S. M., Cao, L., Cui, Y., Gupta, J. A., Gutiérrez, H. R., Heinz, T. F., Hong, S. S., Huang, J., Ismach, A. F., Johnston-Halperin, E., Kuno, M., Plashnitsa, V. V., Robinson, R. D., Ruoff, R. S., Salahuddin, S., Shan, J., Shi, L., Spencer, M. G., Terrones, M., Windl, W. & Goldberger, J. E. Progress, challenges, and opportunities in two-dimensional materials beyond graphene. *ACS Nano* **7**, 2898–2926 (2013).

8 Dean, C. R., Young, A. F., Meric, I., Lee, C., Wang, L., Sorgenfrei, S., Watanabe, K., Taniguchi, T., Kim, P., Shepard, K. L. & Hone, J. Boron nitride substrates for high-quality graphene electronics. *Nat. Nanotechnol.* **5**, 722–726 (2010).

9 Wang, H., Taychatanapat, T., Hsu, A., Watanabe, K., Taniguchi, T., Jarillo-Herrero, P. & Palacios, T. BN/Graphene/BN transistors for RF applications. *IEEE Electron Device Lett.* **32**, 1209–1211 (2011).

10 Watanabe, K., Taniguchi, T. & Kanda, H. Direct-bandgap properties and evidence for ultraviolet lasing of hexagonal boron nitride single crystal. *Nat. Mater.* **3**, 404–409 (2004).

11 Song, L., Ci, L., Lu, H., Sorokin, P. B., Jin, C., Ni, J., Kvashnin, A. G., Kvashnin, D. G., Lou, J., Yakobson, B. I. & Ajayan, P. M. Large scale growth and characterization of atomic hexagonal boron nitride layers. *Nano Lett.* **10**, 3209–3215 (2010).

12 Kim, K. K., Hsu, A., Jia, X., Kim, S. M., Shi, Y., Dresselhaus, M., Palacios, T. & Kong, J. Synthesis and characterization of hexagonal boron nitride film as a dielectric layer for graphene devices. *ACS Nano* **6**, 8583–8590 (2012).

13 Gong, Y., Shi, G., Zhang, Z., Zhou, W., Jung, J., Gao, W., Ma, L., Yang, Y., Yang, S., You, G., Vajtai, R., Xu, Q., MacDonald, A. H., Yakobson, B. I., Lou, J., Liu, Z. & Ajayan, P. M. Direct chemical conversion of graphene to boron- and nitrogen- and carbon-containing atomic layers. *Nat. Commun.* **5**, 3193 (2014).

14 Levendorf, M. P., Kim, C.-J., Brown, L., Huang, P. Y., Havener, R. W., Muller, D. A. & Park, J. Graphene and boron nitride lateral heterostructures for atomically thin circuitry. *Nature* **488**, 627–632 (2012).

15 Koma, A. Van der Waals epitaxy for highly lattice-mismatched systems. *J. Cryst. Growth* **201–202**, 236–241 (1999).

16 Utama, M. I. B., Peng, Z., Chen, R., Peng, B., Xu, X., Dong, Y., Wong, L. M., Wang, S., Sun, H. & Xiong, Q. Vertically aligned cadmium chalcogenide nanowire arrays on muscovite mica: A demonstration of epitaxial growth strategy. *Nano Lett.* **11**, 3051–3057 (2011).

17 Hong, Y. J., Jung, J. W., Lee, W. H., Ruoff, R. S., Kim, K. S. & Fukui, T. Van der Waals epitaxial double heterostructure: InAs/single-layer graphene/InAs. *Adv. Mater.* **25**, 6847–6853 (2013).

18 Mohseni, P. K., Behnam, A., Wood, J. D., Zhao, X., Yu, K. J., Wang, N. C., Rockett, A., Rogers, J. A., Lyding, J. W., Pop, E. & Li, X. Monolithic III – V nanowire solar cells on graphene via direct van der Waals epitaxy. *Adv. Mater.* **26**, 3755–3760 (2014).

19 Utama, M. I. B., Belarre, F. J., Magen, C., Peng, B., Arbiol, J. & Xiong, Q. Incommensurate van der Waals epitaxy of nanowire arrays: A case study with ZnO on muscovite mica substrates. *Nano Lett.* **12**, 2146–2152 (2012).

20 Hong, Y. J. & Fukui, T. Controlled van der Waals heteroepitaxy of InAs nanowires on carbon honeycomb lattices. *ACS Nano* **5**, 7576–7584 (2011).

21 Zhu, Y., Zhou, Y., Utama, M. I. B., de la Mata, M., Zhao, Y., Zhang, Q., Peng, B., Magen, C., Arbiol, J. & Xiong, Q. Solution phase van der Waals epitaxy of ZnO wire arrays. *Nanoscale* **5**, 7242–7249 (2013).

22 Tomioka, K., Yoshimura, M. & Fukui, T. A III–V nanowire channel on silicon for high-performance vertical transistors. *Nature* **488**, 189–192 (2012).

23 Wallentin, J., Anttu, N., Asoli, D., Huffman, M., Åberg, I., Magnusson, M. H., Siefer, G., Fuss-Kailuweit, P., Dimroth, F., Witzigmann, B., Xu, H. Q., Samuelson, L., Deppert, K. & Borgström, M. T. InP nanowire array solar cells achieving 13.8% efficiency by exceeding the ray optics limit. *Science* **339**, 1057–1060 (2013).

24 Kanungo, P. D., Schmid, H., Björk, M. T., Gignac, L. M., Breslin, C., Bruley, J., Bessire, C. D. & Riel, H. Selective area growth of III–V nanowires and their heterostructures on silicon in a nanotube template: towards monolithic integration of nano-devices. *Nanotechnology* **24**, 225304 (2013).

25 Dai, X., Nguyen, B.-M., Hwang, Y., Soci, C. & Dayeh, S. A. Novel heterogeneous integration technology of III–V layers and InGaAs finFETs to silicon. *Adv. Funct. Mater.* **24**, 4420–4426 (2014).

26 Hong, Y. J., Lee, C.-H., Yoon, A., Kim, M., Seong, H.-K., Chung, H. J., Sone, C., Park, Y. J. & Yi, G.-C. Visible-color-tunable light-emitting diodes. *Adv. Mater.* **23**, 3284–3288 (2011).

27 Wang, Y. Electronic properties of two-dimensional hydrogenated and semihydrogenated hexagonal boron nitride sheets. *Phys. Status Solidi-R* **4**, 34–36 (2010).

28 Jo, J., Yoo, H., Park, S.-I., Park, J. B., Yoon, S., Kim, M. & Yi, G.-C. High-resolution observation of nucleation and growth behavior of nanomaterials using a graphene template. *Adv. Mater.* **26**, 2011–2015 (2014).

29 Kresse, G. & Furthmüller, J. Efficient iterative schemes for ab initio total-energy calculations using a plane-wave basis set. *Phys. Rev. B Condens. Matter* **54**, 11169–11186 (1996).

30 Perdew, J. P., Burke, K. & Ernzerhof, M. Generalized gradient approximation made simple. *Phys. Rev. Lett.* **77**, 3865–3868 (1996).

31 Grimme, S. Semiempirical GGA-type density functional constructed with a long-range dispersion correction. *J. Comput. Chem.* **27**, 1787–1799 (2006).

32 Ponce, F. A., Major, J. S., Plano, W. E. & Welch, D. F. Crystalline structure of AlGaN epitaxy on sapphire using AlN buffer layers. *Appl. Phys. Lett.* **65**, 2302–2304 (1994).

33 Grandjean, N., Massies, J., Vennéguès, P., Laügt, M. & Leroux, M. Epitaxial relation-ships between GaN and Al2O3(0001) substrates. *Appl. Phys. Lett.* **70**, 643–645 (1997).

34 Narayan, J., Dovidenko, K., Sharma, A. K. & Oktyabrsky, S. Defects and interfaces in epitaxial ZnO/α-Al2O3 and AlN/ZnO/α-Al2O3 heterostructures. *J. Appl. Phys.* **84**, 2597–2601 (1998).

35 Munshi, A. M., Dheeraj, D. L., Fauske, V. T., Kim, D.-C., van Helvoort, A. T. J., Fimland, B.-O. & Weman, H. Vertically aligned GaAs nanowires on graphite and few-layer graphene: Generic model and epitaxial growth. *Nano Lett.* **12**, 4570–4576 (2012).

36 Wallentin, J., Kriegner, D., Stangl, J. & Borgström, M. T. Au-seeded growth of vertical and in-plane III–V nanowires on graphite substrates. *Nano Lett.* **14**, 1707–1713 (2014).

37 Djurisic, A. B. & Leung, Y. H. Optical properties of ZnO nanostructures. *Small* **2**, 944–961 (2006).

38 Park, W. I., Yi, G.-C., Kim, M. & Pennycook, S. J. ZnO nanoneedles grown vertically on Si substrates by non-catalytic vapor-phase epitaxy. *Adv. Mater.* **14**, 1841–1843 (2002).

39 Wang, X., Yang, S., Wang, J., Li, M., Jiang, X., Du, G., Liu, X. & Chang, R. P. H. Nitrogen doped ZnO film grown by the plasma-assisted metal-organic chemical vapor deposition. *J. Cryst. Growth* **226**, 123–129 (2001).

40 Kim, S., Park, H., Nam, G., Yoon, H., Kim, J. S., Kim, J. S., Son, J. S., Lee, S. H. & Leem, J. Y. Temperature-dependent photoluminescence of boron-doped ZnO nanorods.. *Bull. Korean Chem. Soc.* **34**, 3335–3339 (2013).

41 Trushin, O. S., Kokko, K., Salo, P. T., Hergert, W. & Kotrla, M. Step roughening effect on adatom diffusion. *Phys. Rev. B* **56**, 12135–12138 (1997).

42 Pierre-Louis, O., D'Orsogna, M. R. & Einstein, T. L. Edge diffusion during growth: The kink Ehrlich-Schwoebel effect and resulting instabilities. *Phys. Rev. Lett.* **82**, 3661–3664 (1999).

43 Hong, Y. J., Jung, H. S., Yoo, J., Kim, Y.-J., Lee, C.-H., Kim, M. & Yi, G.-C. Shape-controlled nanoarchitectures using nanowalls. *Adv. Mater.* **21**, 222–226 (2009).

44 Li, H., Cao, J., Zheng, W., Chen, Y., Wu, D., Dang, W., Wang, K., Peng, H. & Liu, Z. Controlled synthesis of topological insulator nanoplate arrays on mica. *J. Am. Chem. Soc.* **134**, 6132–6135 (2012).

45 Lin, M., Wu, D., Zhou, Y., Huang, W., Jiang, W., Zheng, W., Zhao, S., Jin, C., Guo, Y., Peng, H. & Liu, Z. Controlled growth of atomically thin In2Se3 flakes by van der Waals epitaxy. *J. Am. Chem. Soc.* **135**, 13274–13277 (2013).

46 Lee, C.-H., Yi, G.-C., Zuev, Y. M. & Kim, P. Thermoelectric power measurements of wide band gap semiconducting nanowires. *Appl. Phys. Lett.* **94**, 022106 (2009).

Supplementary Information accompanies the paper on the NPG Asia Materials website (http://www.nature.com/am)